



Terminator Habitability: The Case for Limited Water Availability on M-dwarf Planets

Ana H. Lobo¹ , Aomawa L. Shields^{1,2} , Igor Z. Palubski¹, and Eric Wolf^{2,3,4} ¹ University of California, Irvine Department of Physics & Astronomy, 4129 Frederick Reines Hall, Irvine, CA 92697-4575, USA; ahlobo@uci.edu² NASA NExSS Virtual Planetary Laboratory, Seattle, WA 98195, USA³ University of Colorado, Boulder Laboratory for Atmospheric and Space Physics, Department of Atmospheric and Oceanic Sciences, Boulder, CO 80309, USA⁴ NASA GSFC Sellers Exoplanet Environments Collaboration, Greenbelt, MD 20771, USA

Received 2022 April 11; revised 2022 November 21; accepted 2022 December 5; published 2023 March 16

Abstract

Rocky planets orbiting M-dwarf stars are among the most promising and abundant astronomical targets for detecting habitable climates. Planets in the M-dwarf habitable zone are likely synchronously rotating, such that we expect significant day–night temperature differences and potentially limited fractional habitability. Previous studies have focused on scenarios where fractional habitability is confined to the substellar or “eye” region, but in this paper we explore the possibility of planets with terminator habitability, defined by the existence of a habitable band at the transition between a scorching dayside and a glacial nightside. Using a global climate model, we show that for water-limited planets it is possible to have scorching temperatures in the “eye” and freezing temperatures on the nightside, while maintaining a temperate climate in the terminator region, due to reduced atmospheric energy transport. On water-rich planets, however, increasing the stellar flux leads to increased atmospheric energy transport and a reduction in day–night temperature differences, such that the terminator does not remain habitable once the dayside temperatures approach runaway or moist greenhouse limits. We also show that while water-abundant simulations may result in larger fractional habitability, they are vulnerable to water loss through cold trapping on the nightside surface or atmospheric water vapor escape, suggesting that even if planets were formed with abundant water, their climates could become water-limited and subject to terminator habitability.

Unified Astronomy Thesaurus concepts: [Exoplanets \(498\)](#); [Habitable planets \(695\)](#); [Ocean planets \(1151\)](#); [Planetary atmospheres \(1244\)](#); [Planetary science \(1255\)](#); [Exoplanet atmospheres \(487\)](#); [Planetary climates \(2184\)](#); [M dwarf stars \(982\)](#); [M stars \(985\)](#); [Atmospheric clouds \(2180\)](#); [Habitable zone \(696\)](#)

1. Introduction

Rocky planets in the habitable zones of M-dwarf stars are currently among the most promising astronomical targets for planetary climate characterization studies and the detection of habitable surface climates. M dwarfs, which make up $\sim 70\%$ of all stars (Bochanski et al. 2010), are expected to have abundant rocky Earth-sized planets (Mulders et al. 2015). Also, their reduced luminosity results in a habitable zone that is only ~ 0.2 au from the star (Kasting et al. 1993; Kopparapu et al. 2013), which facilitates detection (Nutzman & Charbonneau 2008). While M-dwarf prospects for habitability have been extensively debated (Scalo et al. 2007; Tarter et al. 2007; Shields et al. 2016), over the course of the last decade many of the most promising candidates for habitability have been discovered orbiting M dwarfs, such as TRAPPIST-1 (Gillon et al. 2017), Proxima Centauri (Anglada-Escudé et al. 2016), and TOI-700 (Gilbert et al. 2020). With the recent launch and deployment of the James Webb Space Telescope (JWST), it may soon be possible to characterize the atmospheres of terrestrial planets in the habitable zones of M dwarfs (Kreidberg & Loeb 2016; Morley et al. 2017; Fauchez et al. 2019). In preparation for upcoming observations, it is increasingly important that we understand the full range of possible M-dwarf planetary climates and their prospects for habitability.

The habitable zone’s close proximity to the star implies that the planets are subject to rapid tidal locking, and are likely to be synchronously rotating, such that they have a permanent dayside (Armitage 2009; Barnes 2017). Without incoming radiation, the nightside climate is determined by atmospheric and ocean energy transport, and could be subject to atmospheric collapse (Joshi et al. 1997). On the highly irradiated dayside, meanwhile, greenhouse effects could be amplified with increased atmospheric water vapor content (Ingersoll 1969), potentially leading to a runaway state. Despite the nightside’s inevitable top-of-atmosphere (TOA) radiative deficit, if the day-to-night energy transport is sufficiently intense, it will be possible for a large portion of a synchronously rotating planet to remain above freezing (e.g., Hu & Yang 2014; Genio et al. 2019; Yang et al. 2019b), without entering a runaway greenhouse state. Even neglecting ocean transport, aquaplanet simulations can achieve moderate temperatures on synchronously rotating planets (e.g., Joshi 2003; Merlis & Schneider 2010; Edson et al. 2011). A temperate climate is achievable even when accounting for the longer-wavelength stellar spectra of M dwarfs, which results in changes to key radiative feedbacks (e.g., Shields et al. 2013; Shields et al. 2014; Kopparapu et al. 2016; Shields et al. 2016; Turbet et al. 2016; Komacek & Abbot 2019). Yet, while we can easily simulate an arbitrary habitable M-dwarf planet, the range of habitable planetary configurations is by no means fully constrained, especially when we consider both ocean-covered and land planets.

Water is a minimum requirement for life as we know it. Therefore, we are naturally most interested in the climates of water worlds. Note that our Earth is effectively a water world, even with $\sim 30\%$ of its surface covered by continents. For simplicity, in exoplanet modeling studies, water worlds are

often assumed to be completely ocean-covered worlds, but that is not always necessarily the case, especially for M-dwarf planets. Determining the amount of water expected on a rocky M-dwarf planet in the habitable zone is no simple matter. Among other things, it depends on whether we expect the planets to have formed in situ or to have migrated. Due to the low luminosity of M dwarfs, their ice lines are relatively close to the habitable zone (~ 0.3 au), such that migration in the inner disk could facilitate water-rich habitable-zone planets (Ogihara & Ida 2009). On the other hand, in situ formation of volatile rich planets would be less likely (Lissauer 2007; Raymond et al. 2007, 2022), even when accounting for volatile delivery through the migration of icy planetesimals (Ciesla et al. 2015). There is also a higher risk of water loss for M-dwarf planets, due to early periods of increased stellar flux and energetic flare activity (Ramirez & Kaltenegger 2014; Luger & Barnes 2015; Tian & Ida 2015; Bolmont et al. 2017), as well as periods of intense tidal heating prior to reaching spin-orbit resonance (Barnes et al. 2013). For the purposes of this study, we are specifically interested in moist M-dwarf planets, but it is possible that these could be predominantly water-limited land planets, rather than ocean-covered worlds. Therefore, our study compares both water-rich ocean-covered scenarios and water-limited land-planet scenarios.

The presence of water on the surface of a planet can have a wide range of effects on the climate—for example, altering the surface heat capacity (Cronin & Emanuel 2013; Donohoe et al. 2014). Water also impacts the surface albedo, whether due to low-albedo liquid water or the ice albedo feedback. Water plays a key role in the radiative budget, influencing cloud formation and structure (Stevens 2005), which in turn affects the planetary albedo (Donohoe & Battisti 2011) and greenhouse effect intensity. It can also alter the atmospheric energy transport (Held & Soden 2006) and enhance the local energy storage (Donohoe et al. 2014; Lobo & Bordoni 2020, Lobo & Bordoni 2022), plus it functions as an important greenhouse gas (Held & Soden 2000) with strong positive climate feedback. Due to water’s various climate feedbacks and its effects on the atmospheric structure, the habitable zone of a water-limited Earth twin is broader than that of an aquaplanet Earth (Abe et al. 2011). But while water’s impact on climate is well understood for Earth, many of these fundamental climate feedbacks behave differently on M-dwarf planets, due to the lower frequency of the stellar radiation.

We typically refer to the stellar radiation as the “shortwave” (SW) flux, to distinguish it from a planet’s “longwave” (LW) thermal emissions. However, compared to other stars, M dwarfs have relatively long wavelength emissions. M-dwarf effective temperatures range from 2000 to 3800 K, such that their peak emissions are at near-IR wavelength (Figure 1) and a large fraction of the SW overlaps with the absorption bands for CO_2 and H_2O (Kasting et al. 1993; Selsis et al. 2007). Water’s absorption is particularly important, with multiple absorption bands near the spectra peak. For reference, we plot H_2O absorption in Figure 1, using values from the HITRAN database. This implies that, unlike Earth’s atmosphere, which is predominantly heated from below, due to SW absorption at the surface, a moist M-dwarf planetary atmosphere can be heated at various levels. It is also important to note that ice and snow albedos are lower for IR radiation as well (Dunkle & Bevans 1956), such that the ice albedo feedback is weaker. On M-dwarf planets, the effects of longer-wavelength radiation

result in warmer climates than would be obtained for equal stellar flux from higher-frequency emitters, such as G and F dwarfs (Shields et al. 2013, 2014, 2016). Therefore, the climate response to the increased stellar radiation on M-dwarf planets is not necessarily similar to Earth’s, and climate scenarios must be explored in the context of specific stellar types.

In this paper, we explore climate at the inner edge of the M-dwarf habitable zone, to determine how fractional habitability changes as dayside temperatures start to exceed habitable limits. In particular, we seek to determine whether it is possible to sustain a habitable band at the transition between a scorching dayside and a glacial nightside, a scenario that we refer to as terminator habitability, or whether fractional habitability becomes impossible once the substellar region surface temperatures surpass habitable limits. While there is no broad consensus in terms of a habitable temperature range, here we use a relatively narrow definition, of temperatures between 0°C and 50°C , to provide a more conservative measure and to better track how fractional habitability changes (Shields et al. 2016). Therefore, we are exploring whether planets with a medium or a large day-to-night temperature gradient can exist specifically near the inner edge of the habitable zone, such that the dayside temperatures surpass 50°C , as well as the resultant consequences in terms of climate and fractional habitability.

For this study, we consider Earth-like planets orbiting AD Leonis, which has a spectral classification of M3.5V, such that synchronously rotating planets in its habitable zone are in a slowly rotating regime (Noda et al. 2017; Haqq-Misra et al. 2018). On these planets, the Rossby deformation radius is smaller than the planetary radius, resulting in a dynamical regime with strong convective activity at the substellar point, a thermally direct day-to-night circulation, and roughly symmetric terminator properties. For dimmer M-dwarf stars, the habitable zone can include synchronously rotating planets that are more rapidly rotating, which have distinct dynamical properties, including a stronger mean zonal flow that produces a band-like structure at the equator (e.g., Haqq-Misra et al. 2018). But here we focus on the dynamics relevant to the habitable zones of brighter M dwarfs, which represent the majority of observed M-dwarf stars (Perryman et al. 1997) and host the majority of exoplanets detected so far (according to the NASA Exoplanet Archive).

We use a 3D global climate model to determine whether it is possible to sustain a temperature gradient large enough for a terminator habitability scenario, and to explore the implications of terminator habitability for future climate characterization studies. It is not our goal to precisely quantify the habitable-zone edge, given that its location is dependent on a large range of properties, including planetary radius and surface gravity (Thomson & Vallis 2019; Yang et al. 2019a), among many other factors (see, e.g., Kasting et al. 1993; Kopparapu et al. 2013; Yang et al. 2013, 2014a; Meadows & Barnes 2018); but rather to explore the mechanisms through which the atmosphere responds to increased stellar flux, including changes in the radiative budget and atmospheric energy transport, in order to determine the viability of these surface climate configurations. We begin with a study of water-abundant aquaplanet simulations (Section 3.1), which is followed by a comparison with water-limited land-planet simulations (Section 3.2). Note that, for simplicity, we will define habitability based on surface temperature alone for the majority of the paper, although we

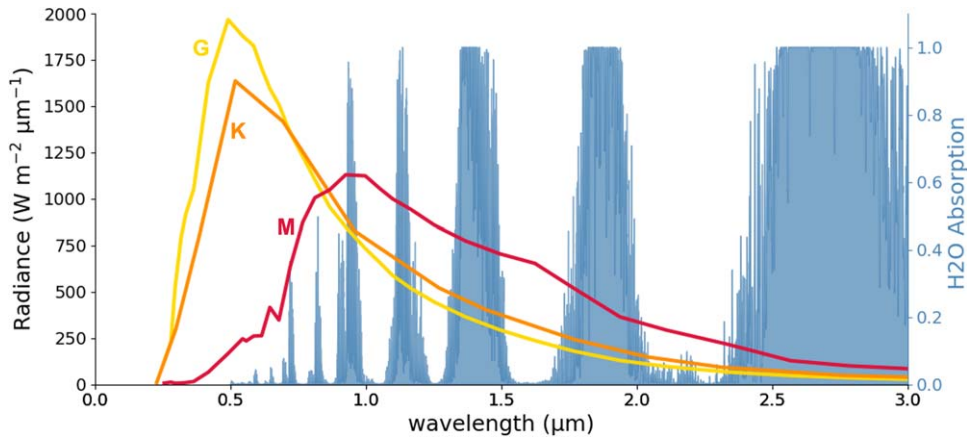


Figure 1. Stellar spectra for AD Leonis (red), HD22049, a K star (orange), and the Sun (yellow). The blue lines show the water absorption values using the Lorentz profile, from the HITRAN database.

discuss long-term water availability and the implications for habitability in Sections 3.3 and 3.4.

2. Methods

In this study, we use ExoCAM (Wolf 2021; Wolf et al. 2022), which is a modified version of the Community Atmosphere Model (CAM4), with correlated-k radiative transfer (ExoRT)⁵ and a finite-volume dynamical core. A complete description of the code and its lineage is available in Wolf et al. (2022 and references therein). In order to isolate the effects of instellation on the day–night temperature contrasts and terminator habitability thresholds, our simulations are Earth-like in terms of radius and gravity, with an atmospheric composition of 40 Pa CO₂, 0.17 Pa CH₄, and the remainder being N₂, totaling 1 bar for the dry component of the atmosphere, with variable H₂O also included. Simulations were run with a horizontal resolution of 4° × 5°, and 40 vertical levels. We use the stellar spectra of AD Leonis (Reid & Gizis 1997; Segura et al. 2005), shown in Figure 1, prescribing zero eccentricity and zero obliquity, such that there is no seasonal cycle. We also calculate the two-band snow and ice albedos (Table 1), which we refer to as the visible (0.25 < λ < 0.75 μm) and near-IR (0.75 < λ < 2.5 μm), weighted by the stellar spectrum.

All simulations use a time step of 1800 s and are run until they reach steady state. The results are shown as a time average of the last 10 years. Two simulations did not reach steady state (Aq25 and Aq25h) and instead failed, due to numeric instabilities, as they entered a runaway greenhouse state. The results for Aq25 are briefly discussed, using the average of the last stable month of model time. The results are shown on a planetary grid, where the substellar point is at 0° longitude and 0° latitude. The figures with a vertical profile use the CESM hybrid sigma-pressure coordinate, plotted on a scale of 0–1, where 1 is the simulation’s reference surface pressure (P_o).

The aquaplanet simulations (Aq) have a uniform 50 m mixed-layer depth and no ocean energy transport. The Aq34 aquaplanet is located 0.15 au from the star. We use this planet as a starting point for our analysis because, for a planet orbiting AD Leonis, this orbital distance results in an Earth-like solar

⁵ During revisions, a minor interpolation error was found and fixed in the ExoCAM ExoRT package (commit 0223865; Wolf 2021). We then ran simulations, branched from the previous spun-up cases, using the updated model. These confirmed that the bug did not impact our results.

Table 1
Albedo Values

| | Visible | Near-IR |
|------|---------|---------|
| Snow | 0.97 | 0.48 |
| Ice | 0.64 | 0.17 |

Table 2
List of Simulations

| Name | Type | P_{orb} (days) | a (au) | F (W m ²) | P_o (bar) |
|--------|--------------|-------------------------|----------|-----------------------|-------------|
| Aq34 | Aquaplanet | 34 | 0.154 | 1378 | 1.0 |
| Aq34h | Aquaplanet | 34 | 0.154 | 1378 | 0.5 |
| Aq30 | Aquaplanet | 30 | 0.141 | 1629 | 1.0 |
| Aq30h | Aquaplanet | 30 | 0.141 | 1629 | 0.5 |
| Aq25 | Aquaplanet | 25 | 0.125 | 2077 | 1.0 |
| Aq25h | Aquaplanet | 25 | 0.125 | 2077 | 0.5 |
| L34Qe3 | $Q = 0.0010$ | 34 | 0.154 | 1378 | 1.0 |
| L34Qe4 | $Q = 0.0001$ | 34 | 0.154 | 1378 | 1.0 |
| L25Qe4 | $Q = 0.0001$ | 25 | 0.125 | 2077 | 1.0 |

constant and a mostly temperate dayside climate. To explore the inner edge of the habitable zone and the transition into runaway greenhouse states, we also use simulations with smaller orbital radii. Per Kepler’s third law, a reduction in orbital radii is accompanied by a change in orbital period, such that

$$P = \left(a^3 \frac{M_{\odot}}{M_{\star}} \right)^{\frac{1}{2}}, \quad (1)$$

where P is the orbital period in years, M_{\star} is the stellar mass, M_{\odot} is the Sun’s mass, and a is the orbital radius in astronomical units. Therefore, to reduce the orbital radii, and increase the stellar flux, we compare simulations with orbital and rotational periods of 34, 30, and 25 days (Table 2). We also include aquaplanet simulations with the atmospheric surface pressure reduced to 0.5 bar (Aqh).

Given our interest in the greenhouse effect, and the enhanced importance of water vapor as an absorber for redder stars, we also use land-planet simulations (L), where the planet’s water is limited. These simulations are initialized without soil or groundwater, with the ground properties of sand everywhere

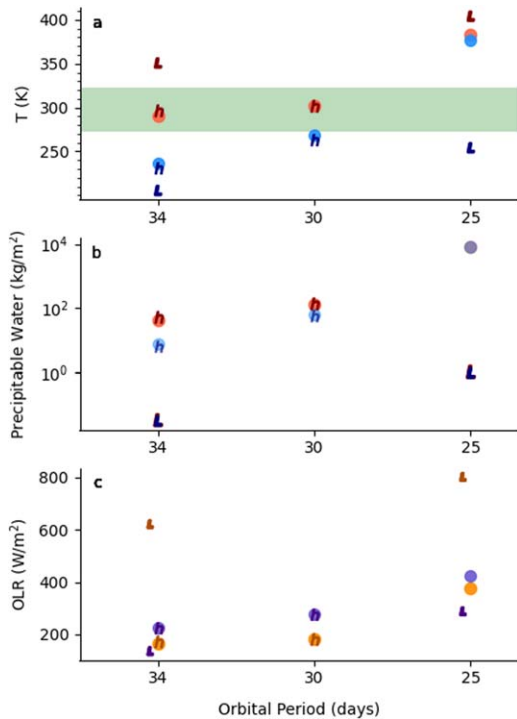


Figure 2. Minimum (blue) and maximum (red) surface temperature (a) and precipitable water (b) for 1 bar (circle) and 0.5 bar (“h”) simulations. The “L” markers show the values for the L34Qe4 and L25Qe4 simulations. The shaded region highlights the temperature range between 0°C and 50°C, where we might expect climate favorable to complex life forms. (c) shows the substellar (orange) and antistellar (purple) TOA OLR values.

(no oceans). All water is initially homogeneously distributed in the atmosphere, where we prescribe the specific humidity (Q). This configuration uses the Community Land Model (Oleson et al. 2010), such that, over time, water can remain in the atmosphere, precipitate, accumulate in the soil, or solidify as snow/ice. We emphasize that these water-limited simulations are significantly different from the aquaplanet simulations, because aquaplanet simulations have unlimited water available for evaporation at each grid box that is not covered in ice.

3. Results

3.1. Water-abundant Worlds

We begin with a simple comparison of the water-abundant cases (Aq34, Aq30, and Aq25), examining the maximum and minimum surface temperatures. By definition, in order for terminator habitability to occur, a planet must sustain large day–night temperature gradients. However, the simulations show that there is a significant reduction in the surface temperature range as the planet moves closer to the star (Figure 2(a)), in agreement with the findings of Yang et al. (2019b), Haqq-Misra et al. (2018), and Noda et al. (2017). Comparing Aq34 and Aq30, we note that Aq30 is on average 25 K warmer, but the day–night temperature contrast (ΔT) is only 34 K (Table 3). This is unfavorable for terminator habitability, because as the planet’s mean temperature increases, the nightside warms more than the dayside, and the day–night contrast becomes small. Therefore, at the inner edge of the habitable zone, we would expect planets to either be mostly habitable (e.g., Figure 3(b)) or, if their temperatures become sufficiently high, entirely uninhabitable, due to a global

Table 3
Planetary Surface Temperatures and fractional habitability (FH)

| | Mean T | T_{\max} | T_{\min} | ΔT | FH 0–50°C |
|--------|----------|------------|------------|------------|-----------|
| Aq34 | 259 K | 291 K | 236 K | 54 K | 32% |
| Aq34h | 257 K | 297 K | 232 K | 66 K | 30% |
| Aq30 | 283 K | 301 K | 268 K | 33 K | 79% |
| Aq30h | 282 K | 302 K | 264 K | 38 K | 75% |
| L34Qe3 | 279 K | 370 K | 248 K | 122 K | 24% |
| L34Qe4 | 247 K | 350 K | 205 K | 145 K | 24% |
| L25Qe4 | 295 K | 404 K | 254 K | 150 K | 16% |

runaway greenhouse effect. In this section, we explore the mechanisms that lead to small day–night temperature differences in the water-abundant planets.

Increasing the mean planetary temperature can result in many changes to the radiative budget, including competing effects. For example, increasing the water vapor contributes to cloud formation and an increase in planetary albedo, which has a strong effect on the climate of M-dwarf planets (Yang et al. 2013; Yang & Abbot 2014). As can be noted in Figure 4(c), regions with abundant clouds reflect a larger fraction of incoming SW, which tends to reduce warming, particularly in the substellar region. Meanwhile, the increased water vapor also leads to stronger LW absorption and a stronger greenhouse effect. But, individually, neither of these effects supports a reduction in the day–night temperature contrast. While the presence of clouds would reduce the dayside warming, the cloud fraction is already high in Aq34, such that there is not a significant difference between the TOA albedo in Aq34 and Aq30. Meanwhile, the increased dayside greenhouse effect on its own, in the absence of any energy and moisture transport, would actually promote increased day–night temperature contrasts. Clearly, that is not what occurs, as can be noted in the surface temperatures (Figure 2(a)) and precipitable water (Figure 2(b)). To fully understand the relationship between the dayside and nightside climates, we have to explore the relationship between the radiative budget and the atmospheric energy transport.

As can be observed for Aq34, in Figure 5(e), (j), and (o), the water vapor (Q) maximizes near the substellar region, and has large values even in the mid-troposphere. The water vapor leads to peaks in SW absorption in the mid- and upper atmospheric layers (Figures 5(c) and (h)), which, when combined with the reflection from clouds, prevents most of the SW from reaching the surface (Figures 5(b), (g), and (i)). The atmospheric substellar absorption of M-dwarf radiation on an Earth-like planet is stronger than for F- or G-dwarf instellation (Shields et al. 2019), such that in this simulation less than 50 W m^{-2} of SW reaches the surface. Even with 400 W m^{-2} of LW, the substellar surface is a radiative local minimum (Figure 5(d)). Near-surface downward radiative flux maxima occur in the “mid-latitudes” (roughly 50° from the substellar point), creating regions of strong evaporation. These are also regions of substantial sensible energy and moisture flux divergence, due to the large-scale overturning circulation’s near-surface winds patterns, such that the “mid-latitude” temperatures are more moderate. Meanwhile, the resulting transport of sensible energy and moisture helps sustain the substellar region’s temperature maxima, despite the weak radiative values.

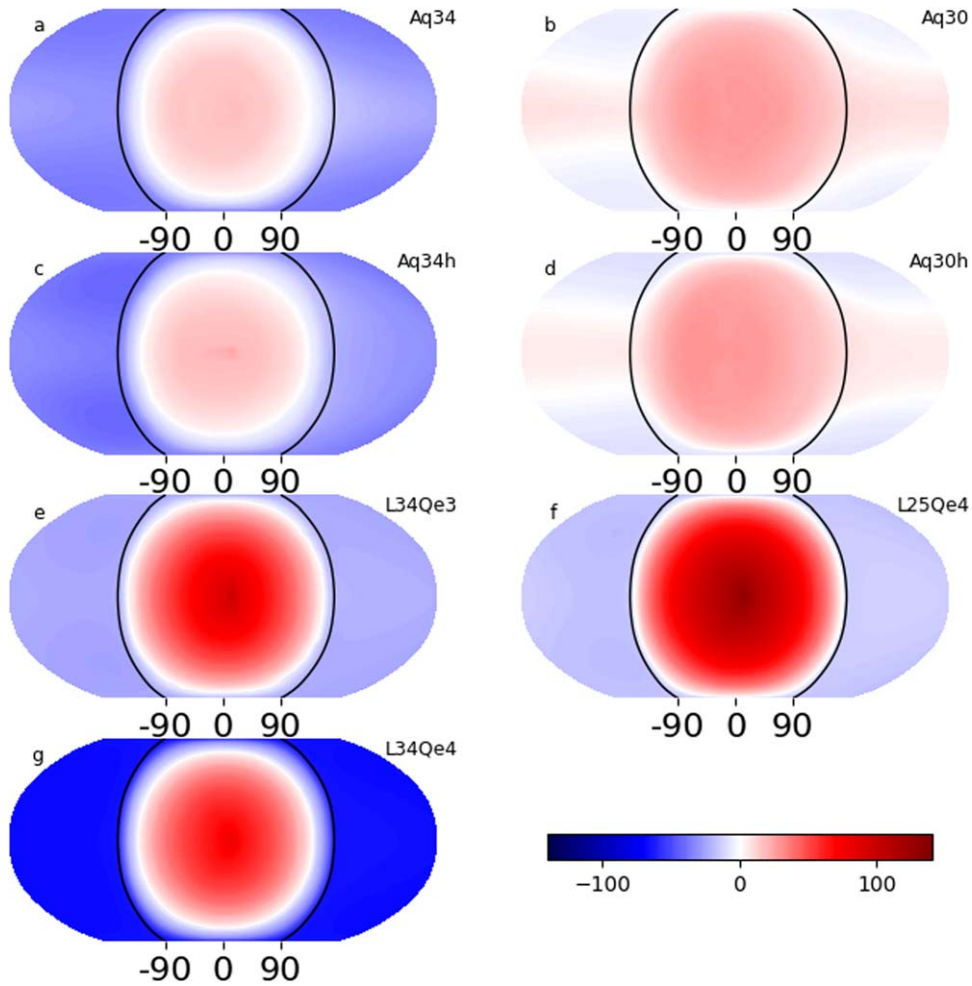


Figure 3. Surface temperatures ($^{\circ}\text{C}$), plotted with the substellar point at the center. The black lines indicate the terminator.

With little SW reaching the surface, and most stellar radiation being absorbed in the mid- and upper atmosphere, we would expect weak atmospheric lapse rates in the aquaplanet simulations. Figure 5(a) shows the atmospheric lapse rates for Aq34, averaged within a 30° radius of the substellar point. The near-surface lapse is roughly adiabatic (8.8 K km^{-1}), and it decreases above the boundary layer in the region of strong convection, as would be expected for a region with moist convection. In the region near $\sigma = 0.5$, where we note strong SW absorption (Figure 5(c)), the lapse rate decreases further, dropping below 4 K km^{-1} at $\sigma = 0.4$. This is significantly lower than the local saturated adiabatic lapse rate of $\sim 7 \text{ K km}^{-1}$, creating a region of convective stability that limits the vertical flow (Figure 6(b)).

Overall, the atmospheric circulation follows a structure typical for a planet in a slowly rotating regime (e.g., Merlis & Schneider 2010; Showman et al. 2013; Haqq-Misra et al. 2018). There is strong near-surface convergence at the substellar region (Figure 4(a)), which drives an upward flow. The flow then diverges in the mid-/upper troposphere (Figure 4(b)), and sinks in the nightside of the planet. But, due to the region of convective stability, the overturning circulation structure is shallow (6(c)), and a second smaller cell forms above the region of convective stability. The divisions between the cell layers are indicated with the black markers in Figure 6(c). If we considered only the cell’s appearance, and the relatively small mass transport, we might erroneously

assume that atmospheric transport plays a reduced role in water-abundant simulations.

While the atmospheric circulation intensity reflects the wind speeds and mass transport, it does not necessarily provide a good indication of the net energy transport. For a planet at steady state, in the absence of ocean energy transport, any TOA imbalance must be equivalent to the vertically integrated atmospheric energy transport, such that the energy budget (e.g., Neelin 2007) for a synchronously rotating planet without a seasonal cycle can be simplified to

$$R_{\text{toa}} - F_{\text{sfc}} = \nabla \cdot \langle \bar{v} \bar{h} \rangle, \quad (2)$$

where R_{toa} is the TOA radiative fluxes and F_{sfc} is the surface fluxes, which include the radiative, sensible, and latent heat flux at the surface. The moist static energy term is defined such that $h = c_p T + L_v Q + gZ$, comprised of dry enthalpy $c_p T$, latent energy $L_v Q$, and potential energy gZ . $\langle \cdot \rangle$ denotes a vertical integral, and $\bar{(\cdot)}$ denotes a temporal long-term average.

As is the case with Earth’s mean meridional circulation, the near-surface convergence of warm air (in this case, at the substellar point) results in the net convergence of dry enthalpy (or sensible energy) and latent energy. The higher-altitude divergent flow (Figure 4(b)) tends to transport colder and dryer air, but with larger amounts of potential energy. On Aq34, both branches transport a significant amount of sensible energy (Figure 7), such that the sensible energy transport partially

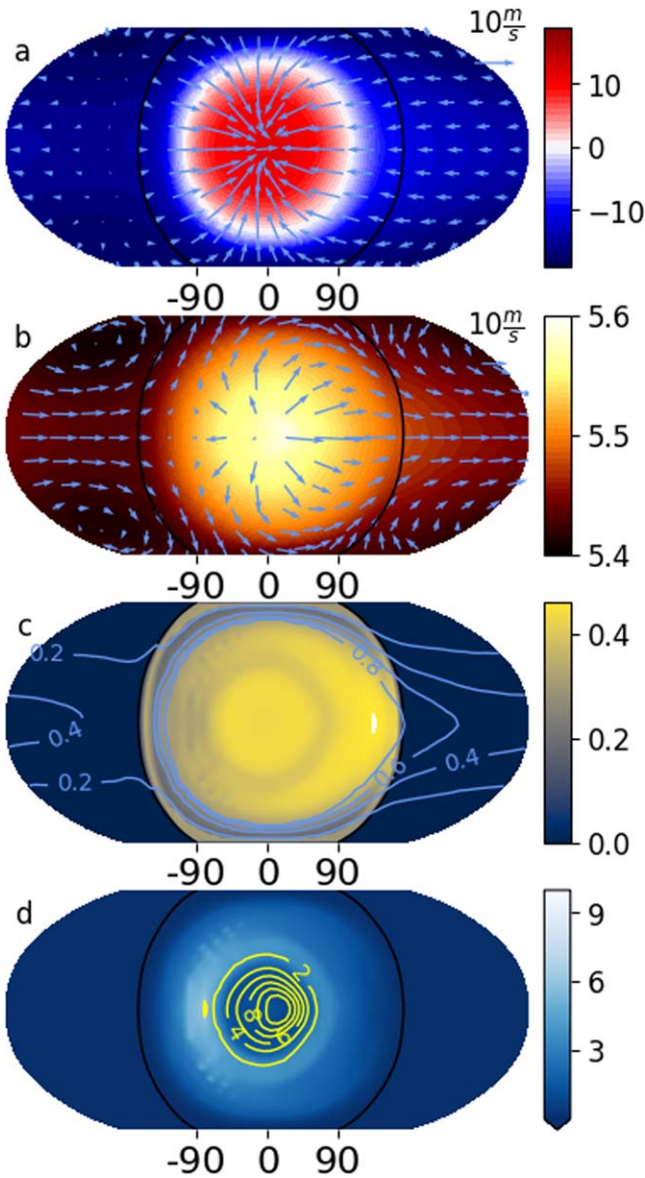


Figure 4. (a) Near-surface ($\sigma = 0.9$) temperatures ($^{\circ}\text{C}$) and wind patterns (quivers). (b) Mid-troposphere ($\sigma = 0.5$) geopotential height (km) and wind patterns (quivers). (c) TOA albedo and vertically integrated total cloud fraction (blue contours). (d) Surface evaporation rates and precipitation reaching the surface (yellow contours; $10^5 \text{ kg m}^{-2} \text{ s}^{-1}$).

cancels out when vertically integrated. The latent energy transport is comparatively small, such that the potential energy transport of the upper branch ultimately determines the sign of the vertically integrated energy transport (Figure 8(a)). The small value of the latent energy flux divergence indicates that while water clearly impacts the overall climate outcome, the latent energy transport has only a small effect on the temperature gradients. The energy flux divergence (the positive values in Figures 7 and 8) indicates net energy transport away from the substellar point.

As we increase the stellar flux (Aq30), the increased dayside SW ($\Delta\text{SW}_{\text{down}}$) is slightly reduced, due to the reflection from the TOA albedo ($\Delta\text{SW}_{\text{up}}$), and balanced, partially by the increased LW (ΔLW), but mostly by the increased energy transport divergence (ΔE). This can be noted in Figure 8(b), which compares Aq30 to Aq34. The net energy transport

remains similar in shape (Figures 8(a) and (c)), but the net sensible energy transport is slightly reduced, in favor of latent and potential energy transport.

Many of the trends noted for Aq30 persist for Aq25. The simulations that do not achieve steady state, as is the case for Aq25, must be interpreted with caution. Prior to reaching numerical instability, the day-to-night temperature differences become nearly negligible (Figure 2(a)). The energy budget is not properly closed, as we might expect for a simulation that is not at steady state. But we notice that the sensible energy transport becomes small, likely due to the reduced temperature gradients, and the majority of the transport is done by the potential and latent energy transport, which increase to similar magnitudes.

In summary, we can attribute the reduction of the day–night temperature differences in our water-abundant planets to an increase in the net energy transport, which leads to additional energy divergence from the dayside, and additional energy convergence to the nightside. In other words, for increased stellar radiation, the transport increases, reducing the intensity of the dayside warming and enhancing the nightside warming. With higher surface and atmospheric temperatures, as well as increased moisture flux convergence, the nightside atmospheric water vapor increases (Figure 2(b)), allowing for additional nightside warming, due to an increase in the local greenhouse effect.

As previously mentioned, the atmospheric energy transport is responsible for resolving radiative imbalances (Equation (2)), such that these changes in the atmospheric transport can be more simply interpreted in the context of the TOA radiative budget. As described in Koll & Abbot (2016), for planets in a weak–temperature gradient regime, the circulation can be thought of as a heat engine driven by dayside heating, with cooling due to global thermal emissions to space. The aquaplanet simulations have high atmospheric water vapor content, resulting in optically thick dayside atmospheres, such that their dayside thermal emissions are determined by the upper-tropospheric temperature. In such cases, increasing the stellar flux has a small impact on the outgoing LW radiation (OLR; Yang & Abbot 2014), as can be noted in Figures 2(c) and 8(b). Meanwhile, the colder nightside has low humidity and a relatively transparent atmosphere (except for Aq25), such that warming is closely tied to increased OLR. Therefore, in a moist and opaque atmosphere, increasing the stellar radiation as we go from Aq34 to Aq30 results in a small dayside OLR increase and a larger nightside OLR increase, requiring a corresponding increase in the day-to-night energy transport. The extra SW absorbed in Aq30 is primarily balanced by a larger nightside OLR, which is only achievable through a strengthening of the atmospheric energy transport and an overall reduction in the day-to-night temperature gradients.

Given that atmospheric energy transport is essential for reducing the day-to-night temperature contrast, we might expect to see larger gradients on planets with thinner atmospheres. However, this is not observed in our aquaplanet simulations where we halve the background N_2 values. As can be noted in Figures 2(a) and 3, the temperature range remains almost unchanged when the surface atmospheric pressure is halved. Instead, we note overall increased wind speeds, such that the energy transport terms remain roughly similar. These results are in general agreement with the findings from Zhang & Yang (2020), which show that the background gas pressure

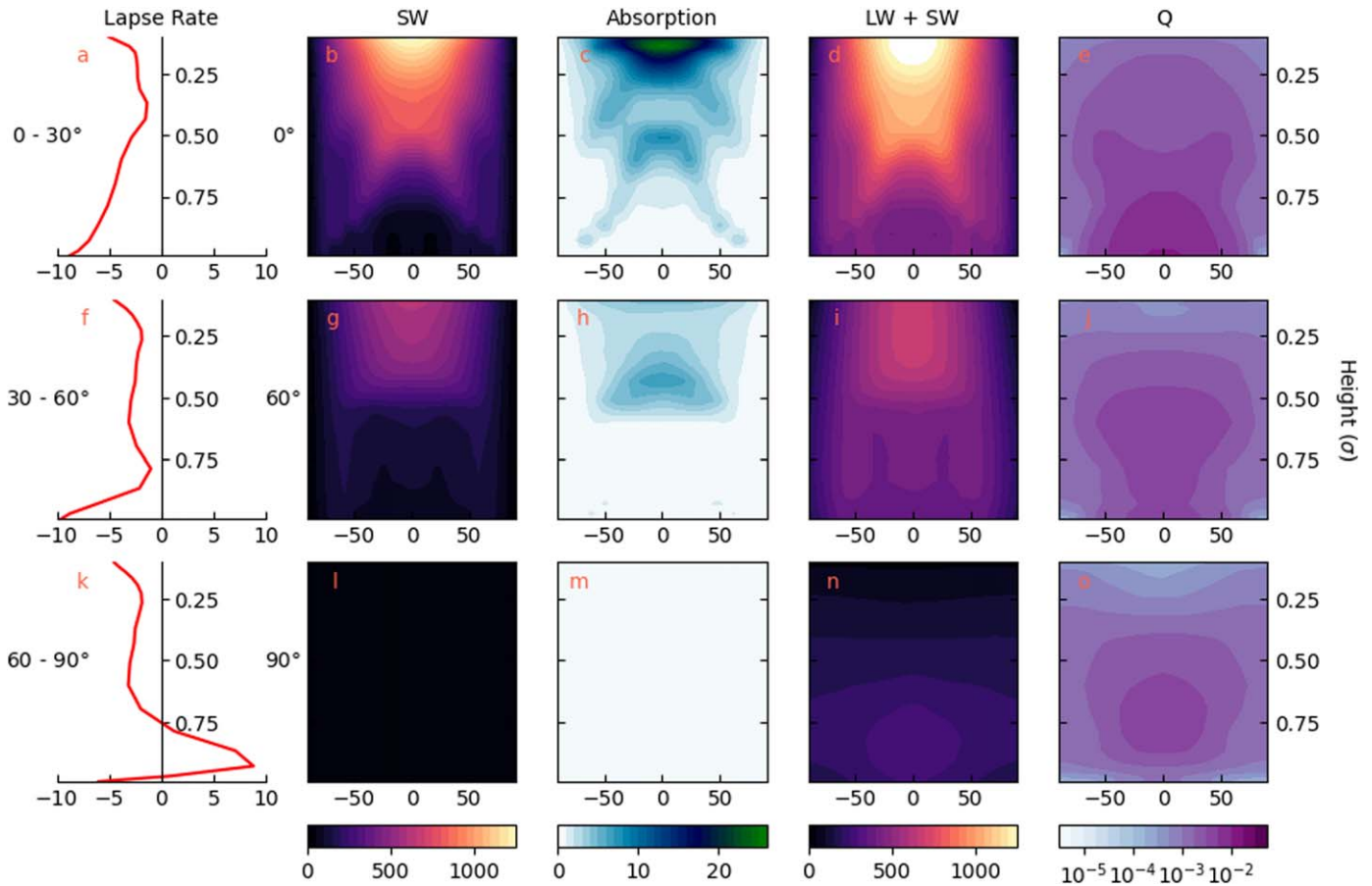


Figure 5. Radiative profiles for Aq34. The left column shows the temperature lapse rate (K km^{-1}), calculated with the area-weighted average of the regions 0° – 30° (a), 30° – 60° (f), and 60° – 90° (k) from the substellar point. The remaining columns, from left to right, show the downward SW (W m^{-2}); the solar heating rate (K day^{-1}); the total downward radiation (SW + LW); and the specific humidity (kg kg^{-1}). The cross sections were taken at longitudes 0° , 60° , and 90° .

has a relatively small impact on the inner edge of the habitable zone for synchronously rotating Earth-like planets. They show that the effects are nonmonotonic, and significantly less important than changes in the cloud scheme (Bin et al. 2018) and rotation rate (Kopparapu et al. 2017). Therefore, we would not expect the pressure alone to determine the viability of terminator habitability for the Earth-like planets that we are considering.

3.2. Water-limited Planets

Here, we switch our focus to water-limited land planets, using ExoCAM with a land-planet setup, initialized with varying amounts of atmospheric water vapor (L34Qe3 and L34Qe4). Once the temperatures equilibrate, these simulations have 20% and 1% of Earth’s atmospheric precipitable water, respectively, also with small amounts of water in the form of surface ice and soil water, concentrated on the nightside. We will begin by considering the differences between L34Qe3 and L34Qe4.

With reduced atmospheric water vapor, we expect a reduction in cloud coverage, especially for low-level clouds. This expectation is confirmed, resulting in a reduction of the dayside albedo, which becomes largely homogeneous with values between 0.2 and 0.26 in the water-limited simulations. There is still some condensation, precipitation, and high-altitude cloud formation, occurring near the substellar point. But with re-evaporation in the atmosphere, the surface

precipitation becomes negligible. These precipitation patterns, noted in all our land-planet simulations, appear to follow the “transition regime” described in Ding & Wordsworth (2021). Despite having the same stellar flux as Aq34, L34Qe4 has a larger net SW, due to the reduced cloud coverage and lower albedo (negative $\Delta\text{SW}_{\text{up}}$; Figure 8(d)). The resulting increase in the substellar net SW must result in one of two outcomes: either increased TOA LW emissions or increased day-to-night energy transport.

Near the substellar point, a much larger fraction of SW reaches the surface (Figure 9), with the dayside surface temperatures reaching maxima of 355K (L34Qe4). Though there is still water vapor SW absorption, the atmosphere’s vertical temperature structure more closely resembles a dry region on Earth, with the dayside lapse rates remaining steeper than 6K km^{-1} until $\sigma = 0.25$ (Figure 6). Without the low region of convective stability noted in Aq34, the water-limited simulations have deeper overturning cells, ascending at the substellar point (Figures 6(f) and (i)).

Examining the energy flux divergence (Figure 8(e)), we note a strengthening of the individual energy transport terms, but a weakening of the net transport. The deepening of the atmospheric circulation, combined with strong high-altitude winds, leads to significantly larger values of potential energy transport away from the “eye,” as can be noted in Figure 7, which shows the vertical profile of the energy flux divergence averaged across an area within 30° of the substellar point. Sensible energy fluxes are intensified in both the upper and

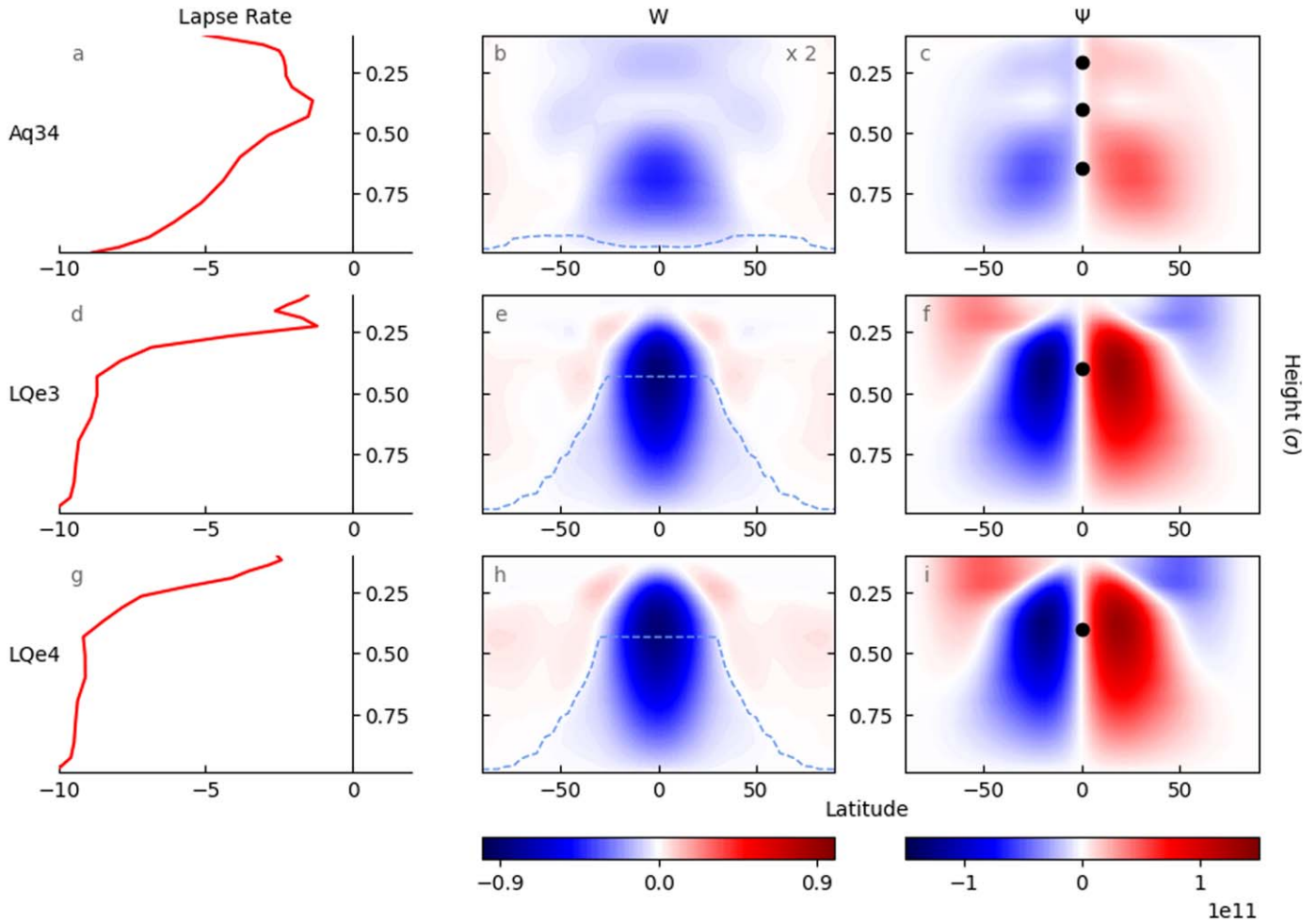


Figure 6. Comparison of aquaplanet (Aq34) and land-planet (L34Qe3 and L34Qe4) simulations with orbital periods of 34 days. The left column shows the atmospheric lapse rate, averaged between 0° and 30° from the substellar point. The middle column shows the vertical velocity (Pa s^{-1}) and the boundary layer depth (the dashed line). The right column shows the mass stream functions (kg s^{-1}), with the black markers indicating the levels where the substellar horizontal flow divergence switches sign. The velocity and stream function cross sections are averaged zonally from -15° to 15° latitude. The vertical velocity values for (b) are multiplied by a factor of 2, to allow for easier comparison.

lower branches of the circulation, but the lower branch increases significantly, in both intensity and depth. The boundary layer in the water-limited simulation is significantly deeper (Figure 7), and the lower branch of the circulation occupies its full depth, reaching up to $\sigma = 0.4$. This effect can also be noted in the upward shift of the cell’s core (Figure 6). This “bottom-heavy” cell structure achieves higher values of sensible heat conversion at the substellar point, which largely cancels out the increased potential energy divergence, such that the net day-to-night energy transport is reduced relative to Aq34, despite the increased net SW. Comparing ΔSW_{up} to the change in net energy flux divergence (ΔE), we note that the effects of the reduced atmospheric energy transport are of comparable intensity to the effects of the reduced albedo.

With reduced albedo and reduced energy transport, the large TOA imbalance is resolved by an increase in the dayside TOA LW emissions (positive ΔLW ; Figure 8(d)). It is interesting to note that in the water-limited cases, the substellar region becomes a region of LW maxima, rather than minima, as was the case for the aquaplanet simulations (Aq34 and Aq30). Meanwhile, the reduced nightside energy convergence results in a reduction of nightside temperatures. Together, these effects allow the water-limited case to achieve equilibrium with larger

day–night temperature gradients, spanning 139 K (L34Qe4) and 122 K (L34Qe3). If we assume that surface temperatures surpassing 50°C are hostile to life, and temperatures nearing 100°C would be uninhabitable, both the L34Qe3 and L34Qe4 water-limited scenarios can be considered as cases of terminator habitability.

As with the aquaplanets, we can reframe these results in terms of the atmospheric radiative imbalances, to obtain a simpler intuition. On these land planets, the atmosphere is dryer, and therefore less cloudy and opaque. This allows the dayside to be closer to radiative equilibrium (Figure 8(d)), which therefore implies reduced energy transport to the nightside. The water-limited L34Qe4 absorbs a greater fraction of the incoming stellar radiation at the surface than Aq34, achieving higher surface temperatures, and higher OLR, which thus requires weaker energy transport (Figure 8(d)). In turn, the nightside receives less energy, and is colder than the aquaplanet counterpart. This results in significantly larger day–night temperature contrasts, such that a temperate terminator becomes not only easily achievable, but also a likely scenario for land planets in the habitable zone.

The simulations discussed so far illustrate the possibility of terminator habitability as an alternative climate configuration

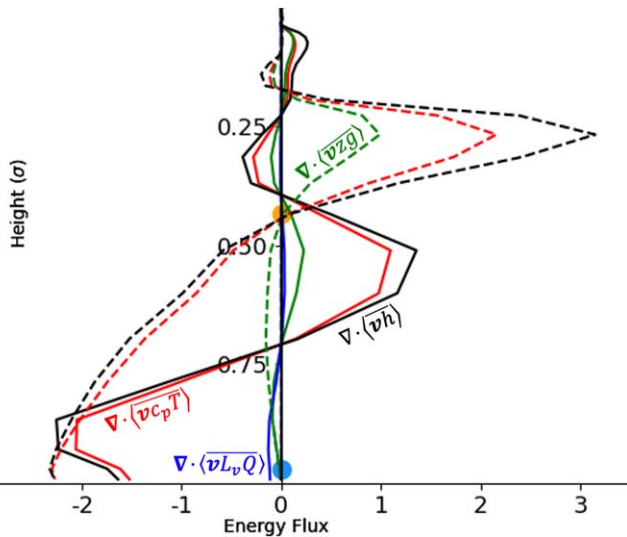


Figure 7. Energy flux divergence in the substellar region, for Aq34 (solid lines) and L34Qe4 (dashed lines). The energy fluxes are broken down into sensible (red), latent (blue), and potential (green) energy components, averaged across an area within 30° latitude of the substellar point, and weighted by a vertical density profile to facilitate a comparison of upper- and lower-level energy transport. The markers show the substellar boundary layer heights for Aq34 (blue) and L34Qe4 (orange).

within the habitable zone (at an orbital period of 34 days). However, it is also worth emphasizing that water-limited planets can endure higher stellar fluxes, without entering a runaway greenhouse state. For example, while Aq25 and Aq25h become unstable due to runaway warming, an equivalent water-limited simulation (L25Qe4) achieves steady state and sustains a temperate terminator climate (Figure 3(f)). The increase in the substellar SW relative to L34Qe4 is balanced in roughly equal parts by an increase in the LW and an increase in the local energy flux divergence. The resulting climate is on average warmer than L34Qe4, and the day-to-night temperature range increases to 154 K (Figure 2). The L25Qe4 nightside temperatures remain just below freezing, the dayside temperatures reach scorching highs over 400 K, and the terminator remains within the 270–320 K range. While the fractional habitability (based on surface temperature) of L25Qe4 may be smaller than those of Aq34 and Aq30 (Table 3), the contrasting results of L25Qe4 and Aq25 illustrate how we might expect to observe planets with diverse surface climates and regions of temperate surface temperatures, even at the inner edge of the habitable zone.

3.3. Long-term Stability

The water-limited simulations show that terminator habitability is possible. However, based on the results discussed so far, we have not yet established whether they are ideal observational targets in the search for life beyond Earth. After all, these simulations depict planets with harsh climates, limited regions of habitability, and limited water availability, which may seem unappealing when compared to the climates of ocean worlds obtained with aquaplanet simulations. However, arid exoplanets offer observational advantages, because their reduced cloud coverage could facilitate the detection of water (Ding & Wordsworth 2022) by JWST, potentially making them more practical near-future targets. Also, a closer look at the aquaplanet moisture budget shows that we must be cautious of

assuming long-term climate stability, which is crucial for increasing the odds of developing life.

Aquaplanet simulations provide the atmosphere with an unlimited water source. On the planet’s dayside, not only is there water available everywhere, but there is no depletion in regions of negative net precipitation, nor resistance to evaporation, as would occur from drying soil (e.g., van de Griend & Owe 1994). For Aq34, which has dayside temperatures comparable to Earth’s, this results in an Earth-like amount of atmospheric precipitable water ($\sim 70\%$ of Earth’s atmospheric water). The “eye” is a region of negative net precipitation, and there is continuous transport of water vapor to the nightside, resulting in a total of $1.5 \times 10^{16} \text{ kg s}^{-1}$ of snowfall. For scale, this rate of snowfall would cold trap a volume of water equivalent to Earth’s oceans in 90,000 years. The presence of a deep global ocean circulation could, in some cases, help deglaciate part or all of the nightside ocean (Hu & Yang 2014). But in the absence of a global ocean with favorable properties, such as large depth (Hu & Yang 2014) and high salinity (Olson et al. 2020), we can assume a limited return flow for water deposited on the nightside. Even accounting for ice sheet dynamics, which would imply a down-gradient flow of ice toward the dayside, it is possible that over time a majority of the water from an ocean-covered Earth-like planet could become cold trapped (Leconte et al. 2013; Menou 2013).

While Aq34 could be at risk for cold trapping, the risk decreases significantly for planets closer to the star. The Aq30 nightside temperatures are higher, such that the equatorial region of the nightside remains above freezing. The snowfall is confined to the higher latitudes, and the global snowfall rate decreases by a factor of 100 relative to Aq34. However, the atmospheric precipitable water increases to approximately 3.5 times the Earth’s atmosphere. In particular, we note an increase in water vapor content above the atmospheric cold trap, reaching values of 0.003 kg kg^{-1} ($\sim 0.005 \text{ mol mol}^{-1}$), which is 2 orders of magnitude larger than the Aq34 values, reaching the limit proposed by Kasting et al. (1984) and confirmed in a series of planetary studies (e.g., Kasting et al. 2015; Wolf & Toon 2015). This raises the possibility that such a planet would be vulnerable to continuous water vapor loss, especially during periods of strong flare activity. These losses are in addition to the water losses resulting from enhanced heating during the M dwarf’s protracted pre-main sequence phase, which could impact all of these scenarios and cause the loss of large water reservoirs (e.g., Luger & Barnes 2015; Bolmont et al. 2017). Therefore, we have abundant reason to question water-rich M-dwarf scenarios.

Meanwhile, for the land planets L34Qe3, L34Qe4, and even L25Qe4, while there is still risk of water loss in their early history, their high-altitude moisture values are comparable to those of Aq34 and well below the Kasting et al. (1984) limit. Similarly, despite their extremely low nightside temperatures, at equilibrium there is no snow being deposited on the nightside. There is some snow and ice accumulation in L34Qe3 while the model spins up, which remains trapped. But the remaining moisture is subsequently retained in the atmosphere above the planetary boundary layer, primarily on the dayside. We have confirmed that simulations initialized with more water (e.g., $Q = 0.01$) have similar nightside water trapping, and slowly tend toward the climate in L34Qe3, but they would

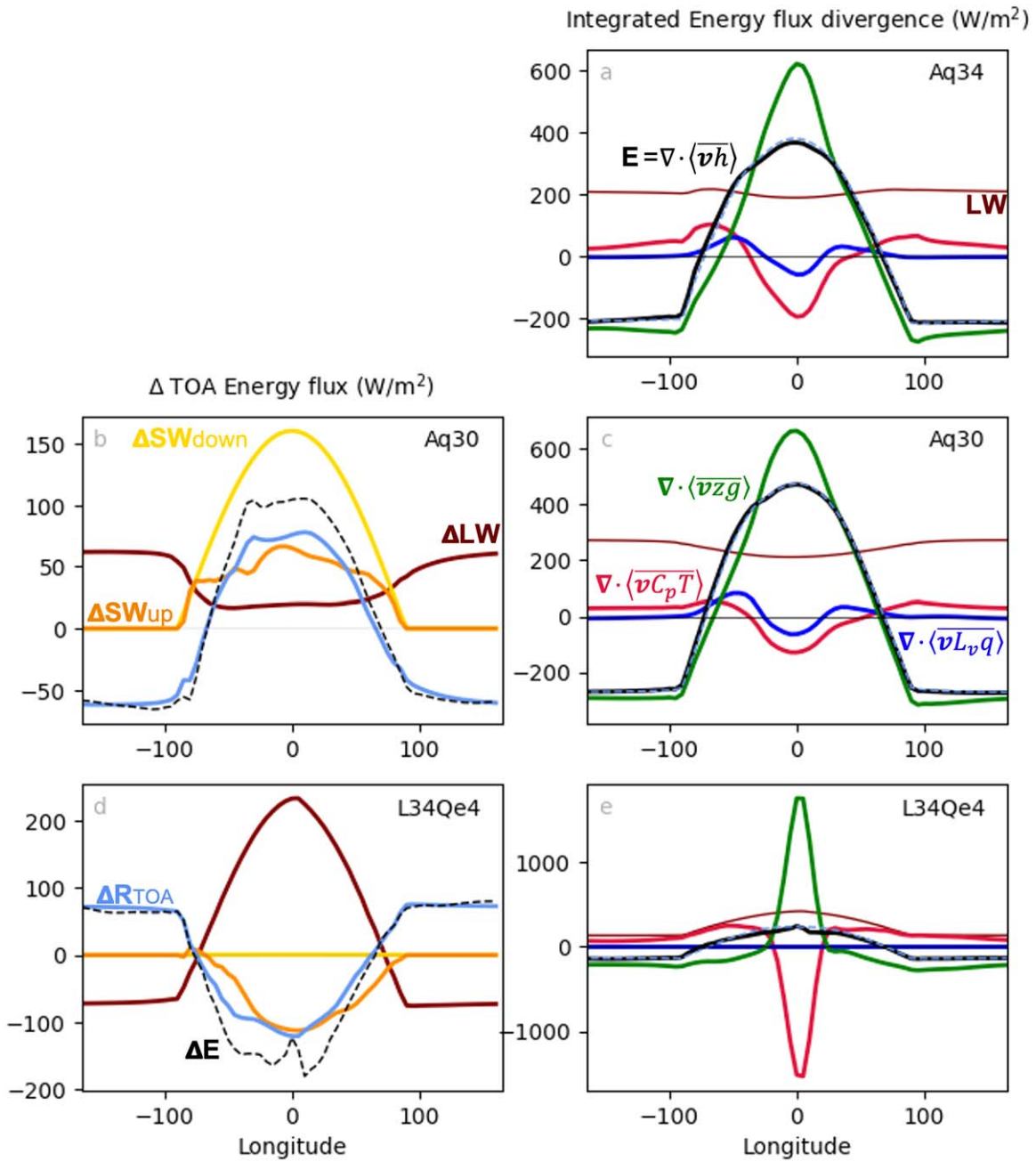


Figure 8. Breakdowns of the planetary energy budget. The left column shows changes in the global mean radiative budget relative to Aq34, such that $\Delta X = X - X_{\text{Aq34}}$, where X is the incoming stellar radiation SW_{down} (yellow), the TOA reflected SW (SW_{up} ; orange), the TOA outgoing LW (maroon), the net TOA radiation (R_{TOA} ; light blue), and the net energy flux divergence ($E = \nabla \cdot \langle \overline{vh} \rangle$; the dashed black line). For each simulation, the actual energy flux divergence values are plotted on the right, broken down into sensible (red), latent (blue), and potential (green) energy components, vertically integrated and meridionally averaged. The thin maroon line shows the TOA upward LW values. We also plot the net atmospheric energy input ($R_{\text{toa}} - F_{\text{scf}}$), as the dashed light blue line, which overlaps with the net energy flux divergence, confirming a closed budget.

require hundreds more simulated years to fully reach equilibrium.

Based on our land-planet simulations, water-limited atmospheres appear to reach a more stable configuration than their aquaplanet counterparts, being less vulnerable to additional water vapor loss or nighttime cold trapping. This also suggests that ocean-world configurations that are subject to significant water loss, without entering a runaway greenhouse state, could eventually reach a stable configuration with terminator habitability. These considerations, combined with the observational advantages of water-limited planets (Ding &

Wordsworth 2022), suggest that despite their potentially limited or localized fractional habitability, land planets will be important observational targets in the coming years, and will play a prominent role in the early stages of exoplanet climate characterization.

3.4. Terminator Water Availability

Thus far, we have defined terminator habitability in terms of surface temperature. However, water is also a crucial ingredient for life as we know it, and could pose a problem for water-

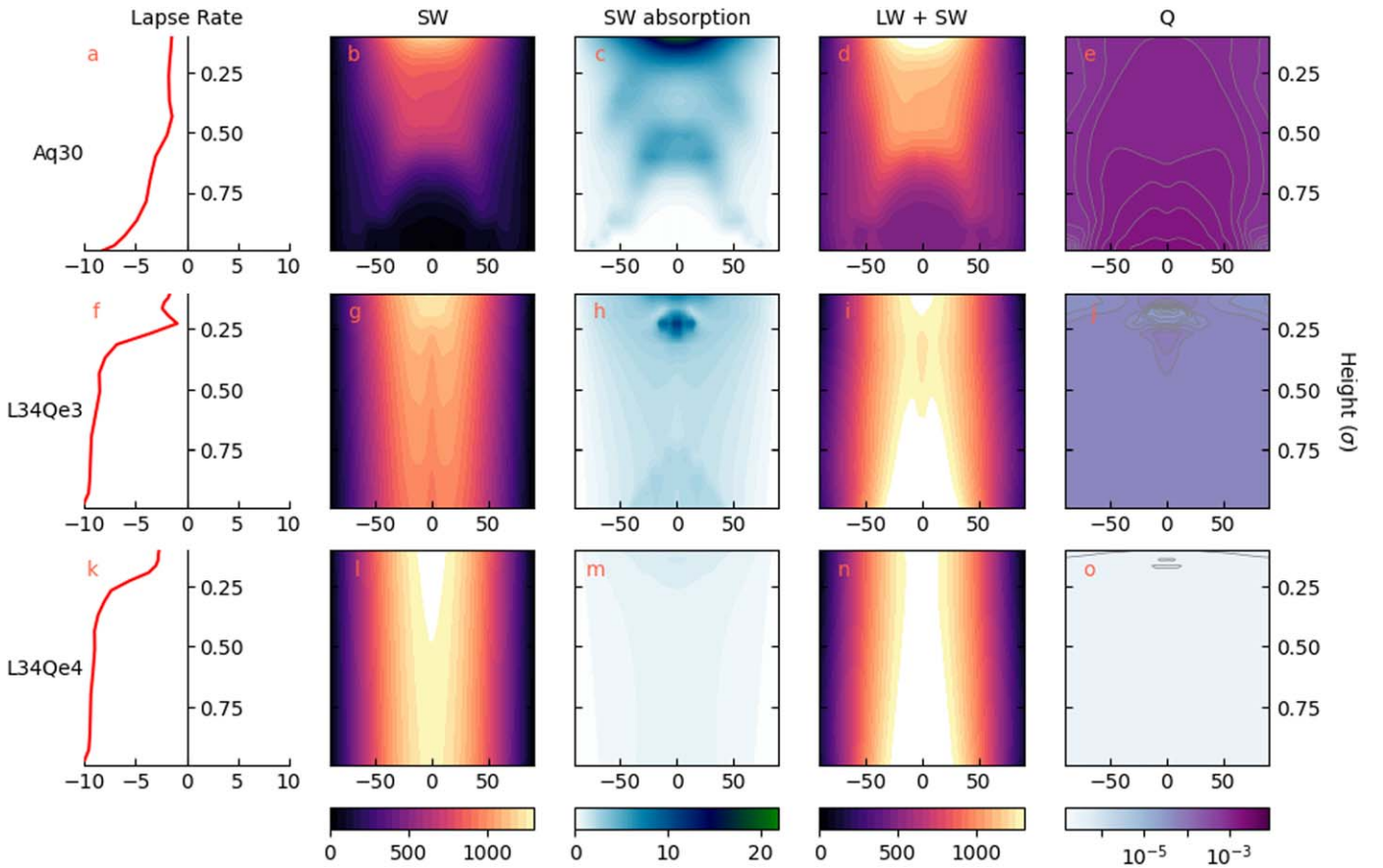


Figure 9. The same as the top row of Figure 5, with each row showing lapse rates averaged over a region 0° – 30° from the substellar point and cross sections taken at 0° longitude for Aq30, L34Qe3, and L34Qe4. To facilitate the comparison across the simulations, the specific humidity is shown on a logarithmic scale.

limited scenarios. In our simulations, rain is strongly concentrated in the substellar region (for both aquaplanet and land-planet simulations), and snow occurs across the nightside in some aquaplanet simulations. For the rotational configurations considered here, the terminator never receives significant amounts of precipitation. Therefore, even though terminator evaporation rates tend to be low, it is a region of weak negative net precipitation in our simulations. In other words, based on the atmospheric moisture budget, the terminator is a region that would tend to have an arid climate. However, water availability on land planets is not exclusively determined by the atmospheric moisture budget, but also depends on factors such as groundwater transport and glacier behavior. These effects are in turn dependent on many poorly constrained planetary properties, such as orography, soil structure, and geothermal heat flux. While we cannot quantify these effects with our climate model, we can discuss them qualitatively, to explore how they would impact the terminator water availability.

The role of glacier flow has been widely discussed, both in the context of a snowball Earth (e.g., Goodman & Pierrehumbert 2003; Pollard & Kasting 2005) and as a potential mechanism for releasing cold-trapped water on synchronously rotating planets (e.g., Leconte et al. 2013). Ice sheets can deform under their own weight, resulting in an ice flow down the ice thickness gradient. On a synchronously rotating planet, this flow could push ice toward the terminator, where the temperate climate would result in melting. The flow velocity depends on, among other things, the ice geometry, planetary gravity, and geothermal heat flux. For super-Earths, Yang et al.

(2014b) argue that it could largely prevent nightside cold trapping on water-abundant planets.

Generally, the ice flow would be slower on Earth-sized planets, especially those with more moderate geothermal heat fluxes, but it could still provide a large enough source of meltwater to create a moist climate in the terminator region. For example, on Greenland and Antarctica, flow speeds and discharge into the ocean can reach rates over 1 km yr^{-1} (Rignot et al. 2011; Rignot & Mouginot 2012). Currently, model representations of glacier dynamics are limited, and not fully suitable for planetary purposes. For CESM, even a configuration with an evolving ice sheet, where the glacier area and elevation are adjusted so as to conserve mass and energy, would not capture the dynamics relevant for the ice flow that we consider here. But, if we make a conservative estimate, considering only the slower flow rates observed at the Antarctic glacier edges ($\sim 100 \text{ m yr}^{-1}$), and assuming that only a shallow ice layer reaches the terminator ($\leq 10 \text{ m}$), this would imply water transport rates on the order of $10^{-2} \text{ kg s}^{-1}$. This exceeds the terminator evaporation rates in the Aq30 and Aq34 simulations (see Figure 4(d)) by 2 orders of magnitude. Given that aquaplanet simulations have infinite water availability, we can cautiously treat their evaporation rates as an upper limit, such that the comparison of glacier flow to aquaplanet terminator evaporation rates indicates that glacier flow could sustain surface water near the terminator. Depending on the exact rates, this could result in swamp-like regions, oceans, or smaller lakes and rivers in regions of topographic lows. Even if the flow rates were significantly lower than expected, and the

surface runoff resulted in a large evaporating area, soil evaporative resistance would tend to retain some local moisture, which could be beneficial for the development of life in the terminator region.

Of course, not all planets would have nightside glaciers. The presence of large ice deposits presumes a planet with abundant initial water, which was either retained throughout the early period of intense stellar emissions or delivered later on. It also presumes that ice would be stable on the nightside. For planets receiving sufficiently high instellation, the nightside ice can sublimate (Ding & Wordsworth 2020), such that water would likely only be present in vapor form. Our arid land-planet simulations are not ideal for exploring this limit, but based on the values from Ding & Wordsworth (2020), we would expect nightside sublimation to be important for planets in L25Qe4’s orbit. Therefore, L25 planets would be more likely to have a temperate but dry terminator than their L30 or L34 counterparts.

A less recognized—but also potentially important—mechanism to consider for planets with stable surface water is groundwater transport. Faulk et al. (2020) have shown that surface and subsurface methane flows on Titan could help to shape the global hydrological cycle, transporting liquid from the low-latitude highlands to the lower polar regions, resulting in a moist polar climate. For synchronously rotating planets, Turbet et al. (2016) have argued that the alignment of large-scale gravitational anomalies and the star–planet axis is favored (Wieczorek 2007), such that the largest topographic basins would tend to be near the substellar point or antistellar point, which has served as motivation for studies of substellar continents on ocean worlds (Lewis et al. 2018). For a land planet, where precipitation is strongly concentrated at the substellar region, a substellar topographic high could result in a hydrological cycle that continuously transports water across a larger portion of the dayside, whereas a topographic low could further concentrate water near the substellar point. Therefore, additional explorations of topography, runoff, and subsurface transport are necessary to constrain the surface water availability for a land planet, especially those with significant large-scale topography.

Based on the above discussion of water availability, we might expect that some, but not all, planets with temperate terminators would also have moist terminator climates. We expect that future work, exploring a wider range of surface configurations, will help to better constrain the water availability for land planets. Model advancements, including glacier dynamics within the water budget, would further improve our understanding of these water worlds. Finally, an important caveat to this work is the fact that we have only considered planets with an Earth-like atmospheric composition. Varying atmospheric mass and composition would certainly impact these results. For example, Ding & Wordsworth (2020) have shown that nightside cold trapping might be avoided on planets with high CO₂ values, due to increased nightside temperatures. Constraining the exoplanet CO₂ levels remains a challenge, due to their dependence on outgassing and weathering rates (Walker et al. 1981). Therefore, future work may wish to consider both terminator habitability and high-CO₂ “eye” habitability scenarios, while exploring additional factors, such as the impact of groundwater flow and long-term climate sensitivity in the presence of M-dwarf flare activity, to quantify prospects for sustained habitability.

4. Conclusions

In this study, we have explored the possibility of terminator habitability, defined as the existence of a habitable band at the transition between a scorching dayside and a glacial nightside on a synchronously rotating Earth-like planet orbiting an M dwarf. In particular, we have explored the viability of this configuration at the inner edge of the habitable zone, to determine whether it is possible for dayside temperatures to exceed typical habitable temperatures, approaching the runaway greenhouse limit, without leading to a planet-wide runaway greenhouse state.




We find that a temperate terminator is not achievable with aquaplanet simulations that seek to reproduce ocean-covered planets, but that it can easily occur on water-limited land planets. On aquaplanets, increasing stellar flux leads to reduced day–night temperature gradients, such that the planet would tend to reach a homogeneous climate before the dayside reaches a runaway greenhouse state, never passing through a terminator habitability state. On water-limited planets, meanwhile, we find that large day–night temperature gradients are easily achievable without entering a runaway greenhouse state. We also find that the water-limited land-planet configurations may be favorable in terms of long-term climate stability, with a reduced risk of nightside water cold trapping or water vapor escape. We expect that water-limited terminator habitability scenarios could be a stable configuration for ocean-covered worlds after significant water loss, especially in the case of nightside cold trapping.

There are still many uncertainties regarding the water content of habitable-zone M-dwarf planets. Based on our current understanding, it is possible that water-limited planets could be abundant and possibly more common than ocean-covered worlds. Therefore, terminator habitability may represent a significant fraction of habitable M-dwarf planets. Compared to the temperate climates obtained with aquaplanets, terminator habitability does offer reduced fractional habitability. Also, while achieving a temperate terminator is relatively easy on water-limited planets, constraining the water availability at the terminator remains a challenge. Overall, the lack of abundant surface water in these simulations could pose a challenge for life to arise under these conditions, but mechanisms, including glacier flow, could allow for sufficient surface water accumulation to sustain locally moist and temperate climates at or near the terminator. We expect that future studies, exploring a broader range of land-planet configurations, in particular those using future generations of surface and ice models, will find a wide range of habitable terminator scenarios in regimes that are intermediate to the water-limited and aquaplanet cases considered here.

This material is based upon work supported by the National Science Foundation, under Award 1753373, and by a Clare Boothe Luce Professorship, supported by the Henry Luce Foundation. This research was also performed as part of NASA’s Virtual Planetary Laboratory, supported by the National Aeronautics and Space Administration, through the NASA Astrobiology Institute, under solicitation NNH12ZDA002C and Cooperative Agreement Number NNA13AA93A, and by the NASA Astrobiology Program, under grant 80NSSC18K0829, as part of the Nexus for Exoplanet System Science (NExSS) research coordination network. We would like to acknowledge the high-performance computing support from Cheyenne (doi: [10.5065/D6RX99HX](https://doi.org/10.5065/D6RX99HX)), provided by NCAR’s Computational and

Information Systems Laboratory, sponsored by the National Science Foundation.

ORCID iDs

Ana H. Lobo  <https://orcid.org/0000-0003-3862-1817>
 Aomawa L. Shields  <https://orcid.org/0000-0002-7086-9516>
 Eric Wolf  <https://orcid.org/0000-0002-7188-1648>

References

- Abe, Y., Abe-Ouchi, A., Sleep, N. H., & Zahnle, K. J. 2011, *AsBio*, **11**, 443
 Anglada-Escudé, G., Amado, P. J., Barnes, J., et al. 2016, *Natur*, **536**, 437
 Armitage, P. J. 2009, *Astrophysics of Planet Formation* (Cambridge: Cambridge Univ. Press)
 Barnes, R. 2017, *CeMDA*, **129**, 509
 Barnes, R., Mullins, K., Goldblatt, C., et al. 2013, *AsBio*, **13**, 225
 Bin, J., Tian, F., & Liu, L. 2018, *E&PSL*, **492**, 121
 Bochanski, J. J., Hawley, S. L., Covey, K. R., et al. 2010, *AJ*, **139**, 2679
 Bolmont, E., Selsis, F., Owen, J. E., et al. 2017, *MNRAS*, **464**, 3728
 Ciesla, F. J., Mulders, G. D., Pascucci, I., & Apai, D. 2015, *ApJ*, **804**, 9
 Cronin, T. W., & Emanuel, K. A. 2013, *JAMES*, **5**, 843
 Ding, F., & Wordsworth, R. D. 2020, *ApJ*, **891**, L18
 Ding, F., & Wordsworth, R. D. 2021, *PSJ*, **2**, 201
 Ding, F., & Wordsworth, R. D. 2022, *ApJL*, **925**, L8
 Donohoe, A., & Battisti, D. S. 2011, *JCLI*, **24**, 4402
 Donohoe, A., Frierson, D. M. W., & Battisti, D. S. 2014, *CIDy*, **43**, 1041
 Dunkle, R. V., & Bevans, J. T. 1956, *JatS*, **13**, 212
 Edson, A., Lee, S., Bannon, P., Kasting, J. F., & Pollard, D. 2011, *Icar*, **212**, 1
 Faucher, T. J., Turbet, M., Villanueva, G. L., et al. 2019, *ApJ*, **887**, 194
 Faulk, S. P., Lora, J. M., Mitchell, J. L., & Milly, P. C. D. 2020, *NatAs*, **4**, 390
 Genio, A. D. D., Way, M. J., Amundsen, D. S., et al. 2019, *AsBio*, **19**, 99
 Gilbert, E. A., Barclay, T., Schlieder, J. E., et al. 2020, *AJ*, **160**, 116
 Gillon, M., Triaud, A. H. M. J., Demory, B.-O., et al. 2017, *Natur*, **542**, 456
 Goodman, J. C., & Pierrehumbert, R. T. 2003, *JGR*, **108**, 3308
 Haqq-Misra, J., Wolf, E. T., Joshi, M., Zhang, X., & Kopparapu, R. K. 2018, *ApJ*, **852**, 67
 Held, I. M., & Soden, B. J. 2000, *Annu. Rev. Energy Environ.*, **25**, 441
 Held, I. M., & Soden, B. J. 2006, *JCLI*, **19**, 5686
 Hu, Y., & Yang, J. 2014, *PNAS*, **111**, 629
 Ingersoll, A. P. 1969, *JatS*, **26**, 1191
 Joshi, M. 2003, *AsBio*, **3**, 415
 Joshi, M., Haberle, R., & Reynolds, R. 1997, *Icar*, **129**, 450
 Kasting, J. F., Chen, H., & Kopparapu, R. K. 2015, *ApJ*, **813**, L3
 Kasting, J. F., Pollack, J. B., & Ackerman, T. P. 1984, *Icar*, **57**, 335
 Kasting, J. F., Whitmire, D. P., & Reynolds, R. T. 1993, *Icar*, **101**, 108
 Koll, D. D. B., & Abbot, D. S. 2016, *ApJ*, **825**, 99
 Komacek, T. D., & Abbot, D. S. 2019, *ApJ*, **871**, 245
 Kopparapu, R. K., Wolf, E. T., Arney, G., et al. 2017, *ApJ*, **845**, 5
 Kopparapu, R. K., Wolf, E. T., Haqq-Misra, J., et al. 2016, *ApJ*, **819**, 84
 Kopparapu, R. K., Ramirez, R., Kasting, J. F., et al. 2013, *ApJ*, **765**, 131
 Kreidberg, L., & Loeb, A. 2016, *ApJ*, **832**, L12
 Lecointe, J., Forget, F., Charnay, B., et al. 2013, *A&A*, **554**, A69
 Lewis, N. T., Lambert, F. H., Boule, I. A., et al. 2018, *ApJ*, **854**, 171
 Lissauer, J. J. 2007, *ApJ*, **660**, L149
 Lobo, A. H., & Bordononi, S. 2020, *Icar*, **340**, 4
 Lobo, A. H., & Bordononi, S. 2022, *JGRD*, **127**, e2021JD036003
 Luger, R., & Barnes, R. 2015, *AsBio*, **15**, 119
 Meadows, V. S., & Barnes, R. K. 2018, *Handbook of Exoplanets* (Switzerland: Springer), 2771
 Menou, K. 2013, *ApJ*, **774**, 51
 Merlis, T. M., & Schneider, T. 2010, *JAMES*, **2**, 13
 Morley, C. V., Kreidberg, L., Rustamkulov, Z., Robinson, T., & Fortney, J. J. 2017, *ApJ*, **850**, 121
 Mulders, G. D., Pascucci, I., & Apai, D. 2015, *ApJ*, **814**, 130
 Neelin, J. D. 2007, *The Global Circulation of the Atmosphere* (Princeton, NJ: Princeton Univ. Press), 267
 Noda, S., Ishiwatari, M., Nakajima, K., et al. 2017, *Icar*, **282**, 1
 Nutzman, P., & Charbonneau, D. 2008, *PASP*, **120**, 317
 Ogihara, M., & Ida, S. 2009, *ApJ*, **699**, 824
 Olson, S. L., Jansen, M., & Abbot, D. S. 2020, *ApJ*, **895**, 19
 Oleson, K. W., Lawrence, D. M., Bonan, G. B., et al. 2010, Technical Description of version 4.0 of the Community Land Model (CLM), *University Corporation for Atmospheric Research*
 Perryman, M. A. C., Lindegren, L., Kovalevsky, J., et al. 1997, *A&A*, **323**, L49
 Pollard, D., & Kasting, J. F. 2005, *JGRC*, **110**, C07010
 Ramirez, R. M., & Kaltenegger, L. 2014, *ApJ*, **797**, L25
 Raymond, S. N., Scalo, J., & Meadows, V. S. 2007, *ApJ*, **669**, 606
 Raymond, S. N., Izidoro, A., Bolmont, E., et al. 2022, *NatAs*, **6**, 80
 Reid, I. N., & Gizis, J. E. 1997, *AJ*, **113**, 2246
 Rignot, E., & Mougnot, J. 2012, *GeoRL*, **39**, L11501
 Rignot, E., Mougnot, J., & Scheuchl, B. 2011, *Sci*, **333**, 1427
 Scalo, J., Kaltenegger, L., Segura, A., et al. 2007, *AsBio*, **7**, 85
 Segura, A., Kasting, J. F., Meadows, V., et al. 2005, *AsBio*, **5**, 706
 Selsis, F., Kasting, J. F., Levrard, B., et al. 2007, *A&A*, **476**, 1373
 Shields, A. L., Ballard, S., & Johnson, J. A. 2016, *PhR*, **663**, 1
 Shields, A. L., Bitz, C. M., Meadows, V. S., Joshi, M. M., & Robinson, T. D. 2014, *ApJ*, **785**, L9
 Shields, A. L., Bitz, C. M., & Palubski, I. 2019, *ApJL*, **884**, L2
 Shields, A. L., Meadows, V. S., Bitz, C. M., et al. 2013, *AsBio*, **13**, 715
 Showman, A. P., Wordsworth, R. D., Merlis, T. M., & Kaspi, Y. 2013, *Atmospheric Circulation of Terrestrial Exoplanets, Comparative Climatology of Terrestrial Planets* (Tucson, AZ: Univ. Arizona Press)
 Stevens, B. 2005, *AREPS*, **33**, 605
 Tarter, J. C., Backus, P. R., Mancinelli, R. L., et al. 2007, *AsBio*, **7**, 30
 Thomson, S. I., & Vallis, G. K. 2019, *QJRM*, **145**, 2627
 Tian, F., & Ida, S. 2015, *NatGe*, **8**, 177
 Turbet, M., Leconte, J., Selsis, F., et al. 2016, *A&A*, **596**, A112
 van de Griend, A. A., & Owe, M. 1994, *WRR*, **30**, 181
 Walker, J. C. G., Hays, P. B., & Kasting, J. F. 1981, *JGR*, **86**, 9776
 Wieczorek, M. 2007, *Treatise on Geophysics*, Vol. 10 (Amsterdam: Elsevier), 165
 Wolf, E. 2021, *GitHub repository*, <https://github.com/storyofthewolf/ExoCAM>
 Wolf, E. T., Kopparapu, R., Haqq-Misra, J., & Faucher, T. J. 2022, *PSJ*, **3**, 7
 Wolf, E. T., & Toon, O. B. 2015, *JGRD*, **120**, 5775
 Yang, H., Komacek, T. D., & Abbot, D. S. 2019a, *ApJ*, **876**, L27
 Yang, J., Abbot, D. S., Koll, D. D. B., Hu, Y., & Showman, A. P. 2019b, *ApJ*, **871**, 29
 Yang, J., & Abbot, D. S. 2014, *ApJ*, **784**, 155
 Yang, J., Boué, G., Fabrycky, D. C., & Abbot, D. S. 2014a, *ApJ*, **787**, L2
 Yang, J., Liu, Y., Hu, Y., & Abbot, D. S. 2014b, *ApJ*, **796**, L22
 Yang, J., Cowan, N. B., & Abbot, D. S. 2013, *ApJ*, **771**, L45
 Zhang, Y., & Yang, J. 2020, *ApJ*, **901**, L36